Joule

CellPress
OPEN ACCESS

Article

Photoprotection in metal halide perovskites by ionic defect formation

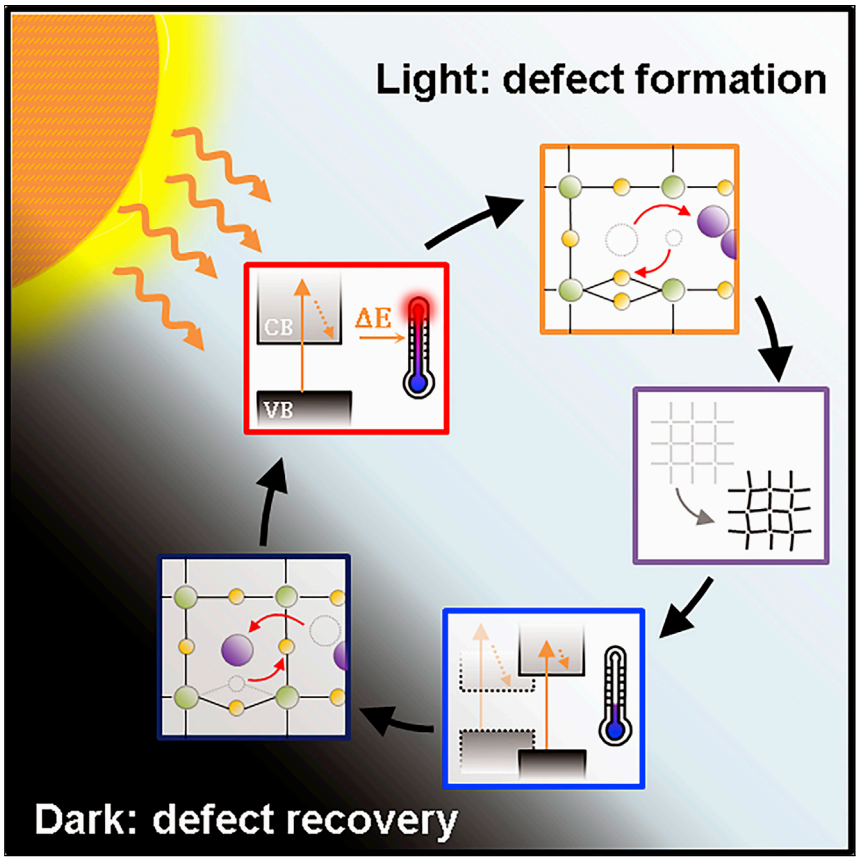

Metal halide perovskites form defects as a response to intense light in order to protect themselves from overheating and degrading. The defects in turn alter the material properties to limit photon absorption, and thereafter, the defects gradually recover and restore the optoelectronic properties. In plants, mechanisms to reduce radiation damage serve the purpose of temporarily limiting the photon dose, and thereby photosynthesis, in order to improve photostability. Such a feature in halide perovskites is promising for their photovoltaic applications.

Nga Phung, Alessandro Mattoni, Joel A. Smith, ..., Simone Meloni, Antonio Abate, Aboma Merdasa

simone.meloni@unife.it (S.M.)
antonio.abate@unina.it (A.A.)
aboma.merdasa@med.lu.se (A.M.)

Highlights

Formation of photoinduced ionic defects reduces the thermal impact on the absorber

Defect formation and recovery trigger processes that regulate photon absorption

Demonstrated photostability of perovskite films under intense flux above 10^4 sun

Long-term photostability of devices demonstrated under 5-sun concentrated sunlight

Phung et al., Joule 6, 2152–2174
September 21, 2022
Published by Elsevier Inc.
https://doi.org/10.1016/j.joule.2022.06.029

CellPress
OPEN ACCESS

Joule

Article

Photoprotection in metal halide perovskites by ionic defect formation

Nga Phung,[1,13] Alessandro Mattoni,[4] Joel A. Smith,[1,5,14] Dieter Skroblin,[6] Hans Köbler,[1] Leo Choubrac,[2] Joachim Breternitz,[2] Jinzhao Li,[3] Thomas Unold,[2] Susan Schorr,[2] Christian Gollwitzer,[6] Ivan G. Scheblykin,[7] Eva L. Unger,[3,7] Michael Saliba,[8,9] Simone Meloni,[10,*] Antonio Abate,[1,11,*] and Aboma Merdasa[3,12,15,*]

SUMMARY

Photostability is critical for long-term solar cell operation. While light-triggered defects are usually reported as evidence of material degradation, we reveal that the formation of certain defects in metal halide perovskites is crucial for protection against intense or prolonged light exposure. We identify an inherent self-regulating cycle of formation and recovery of ionic defects under light exposure that mitigates the overheating of the lattice due to hot carrier cooling, which allows exposure to several thousand suns without degrading. The excess energy instead dissipates by forming defects, which in turn alters the optoelectronic properties of the absorber, resulting in a temporary reduction of photon absorption. Defects gradually recover to restore the original optoelectronic properties of the absorber. Photoprotection is a key feature for the photostability in plants. Thus, finding a protection mechanism in metal halide perovskites similar to those in nature is encouraging for the development of long-term sustainable solar cells.

INTRODUCTION

Metal halide perovskites have generated much excitement for optoelectronic devices because of their intriguing material properties. After more than a decade of developing perovskite-based devices, impressive performances have been achieved in both light-emitting diodes (LEDs) and photovoltaic (PV) applications.[1] However, long-term material photostability remains the primary roadblock for commercial success. Current research relates the poor photostability to the seemingly low barrier at which ionic defects in the absorber form and migrate when exposed to light.[2] Nevertheless, emerging studies show that these defects in some perovskite compounds can recover given sufficient time to rest in the dark.[3–5] This requires a re-evaluation of the photostability of metal halide perovskites and its relation to ionic defects.

In this work, we uproot the common understanding of perovskite photostability. We argue that the inherent ability of halide perovskite to form ionic defects when exposed to light, and to subsequently sustain a large concentration of defects,[6] protects the absorber from irreversibly degrading. Through a series of *in situ* experiments, supported by theoretical calculations, we demonstrate that ionic defect formation serves as a protective response to the excess absorbed photon energy that would otherwise thermalize and detrimentally heat the lattice. At the same time, the presence of defects widens the band gap, which in turn reduces the photon

CONTEXT & SCALE

Photoprotection is a vital phenomenon in plants that, under intense and prolonged exposure to light, temporarily limits photon absorption to avoid radiation damage, which allows long-term stable and efficient photosynthesis. Photoprotection has only been linked to organisms; however, we discover a parallel mechanism in metal halide perovskite semiconductors. When perovskite films are exposed to light, a process involving the formation of defects is initiated, which protects the film from overheating and degradation.

Defect formation in perovskites is generally undesired, as it leads to a loss of optoelectronic performance. We not only argue that this efficiency loss is temporary but also that it is in fact critical for long-term photostability. Perovskites retain material integrity under intense flux, as defects easily form and the lattice can sustain a large concentration of them. Thus, whether defect formation in perovskites should be mitigated or preserved is a topic requiring further consideration.

absorption and the thermalization energy. When the defects recover, both the structure and electronic properties of the absorber are restored. Hence, defect formation plays a critical role in a self-regulating photoprotection mechanism that reduces the indirect thermal impact by photon absorption and thereby prevents the perovskite absorber from permanently degrading.

We demonstrate the effectiveness of this self-regulating photoprotection mechanism in perovskite thin films showing a resistance toward degradation, despite exposure to photon fluxes over 10^3 W/cm^2, while the local film temperature in the illumination spot only rises a few K above room temperature during exposure. Additionally, we show a complete recovery of a seemingly degraded thin film exposed to 10^5 W/cm^2 relating it to the formation and recovery of specific ionic defects. Thus, despite the commonly reported harmful effect of defects on the stability of halide perovskites,[7] our results suggest that the formation of defects is a beneficial process for photostability, provided that conditions for the defects to recover exist. Although the presence of pre-existing defects do deteriorate optoelectronic properties, the formation of defects under light exposure and subsequent recovery in dark are key processes in an inherent defense mechanism that should be preserved, rather than mitigated. Intriguingly, photoprotection mechanisms can also be found in nature, where, for example, plant leaves protect themselves from excess irradiation and damaging heat through various photophysical and chemical excess-energy-dissipation processes.[8–10]

RESULTS AND DISCUSSION

Light-induced ionic defect formation

We focus on the archetypal methylammonium lead iodide ($MAPbI_3$) perovskite because of its compositional simplicity and well-established structural and optical properties, which allow us to ensure a robust theoretical framework against which experimental observations could be compared.

A continuous wave (CW) diode laser with excitation wavelength λ_{ex} = 450 nm (2.75 eV) and maximum excitation power of 2.48 mW was used to excite a polycrystalline $MAPbI_3$ thin film in a homebuilt photoluminescence (PL) microscope. The excitation power density was obtained as a function of distance from the center of the spot (Note S1), with a maximum excitation power density of 3.1 kW/cm^2 (~30,000 suns) in the center. Here, we focus on high photon energies and discuss the dependence on photon energy below. During exposure, PL spectra were recorded every 50 ms and fitted with an asymmetric Voigt line shape to track the PL peak position in time. Figure 1A shows the rather dynamic behavior of the PL peak position upon light exposure where the initial red shift (<1 s) is likely related to the rearrangement and aligning of the methylammonium (MA) cations.[11] This dynamic behavior of the organic cation has been widely reported both from a theoretical calculation point of view and evidence from experimental results.[11,12] Here, we refrain from discussing this fast initial drop in detail and focus on the following gradual shift of the peak toward higher energies over the following 10–15 s, which is of more interest. The PL shifts are on the order of a few meVs, from which the emission can primarily be assumed to reflect a generally intact perovskite structure.

Figure 1A indicates that no significant degradation of the perovskite occurs in the excited spot during illumination with ~30,000 suns, which is remarkable considering previously reported temperature rises under far lower photon fluxes.[13] This is supported by extended exposure up to 100 s with no noticable peak shifts and no

[1]Department of Novel Materials and Interfaces for Photovoltaic Solar Cells, Helmholtz-Zentrum Berlin für Materialien und Energie GmbH, Kekulestraße 5, 12489 Berlin, Germany

[2]Department of Structure and Dynamics of Energy Materials, Helmholtz-Zentrum Berlin für Materialien und Energie GmbH, Hahn-Meitner Platz 1, 14109 Berlin, Germany

[3]Department Solution Processing of Hybrid Materials & Devices, Helmholtz-Zentrum Berlin für Materialien und Energie GmbH, Kekulestraße 5, 12489 Berlin, Germany

[4]Consiglio Nazionale delle Ricerche, Istituto Officina dei Materiali, CNR-IOM, Cagliari, Cittadella Universitaria, Monserrato, 09042 Cagliari, Italy

[5]Department of Physics and Astronomy, University of Sheffield, Hicks Building, Hounsfield Road, Sheffield S3 7RH, UK

[6]Physikalisch-Technische Bundesanstalt (PTB), Abbestraße 2-12, 10587 Berlin, Germany

[7]Department of Chemistry and NanoLund, Lund University, Naturvetarvägen 14, 22362 Lund, Sweden

[8]Institute for Photovoltaics (IPV), University of Stuttgart, Pfafenwaldring 47, 70569 Stuttgart, Germany

[9]Helmholtz Young Investigator Group FRONTRUNNER, IEK5-Photovoltaik Forschungszentrum Jülich, 52425 Jülich, Germany

[10]Dipartimento di Scienze Chimiche, Farmaceutiche e Agrarie (DOCPAS), Università degli Studi di Ferrara (Unife), Via Luigi Borsari 46, 44121 Ferrara, Italy

[11]Department of Chemical, Materials and Production Engineering, University of Naples Federico II, Piazzale Tecchio 80, 80125 Fuorigrotta, Italy

[12]Department of Clinical Sciences Lund, Lund University, Sölvegatan 19, 22362 Lund, Sweden

[13]Present address: Department of Applied Physics, Eindhoven University of Technology, 5600 MB Eindhoven, the Netherlands

[14]Present address: Department of Physics, University of Oxford, Parks Road, Oxford OX1 3PU, UK

[15]Lead contact

*Correspondence: simone.meloni@unife.it (S.M.), antonio.abate@unina.it (A.A.), aboma.merdasa@med.lu.se (A.M.)

https://doi.org/10.1016/j.joule.2022.06.029

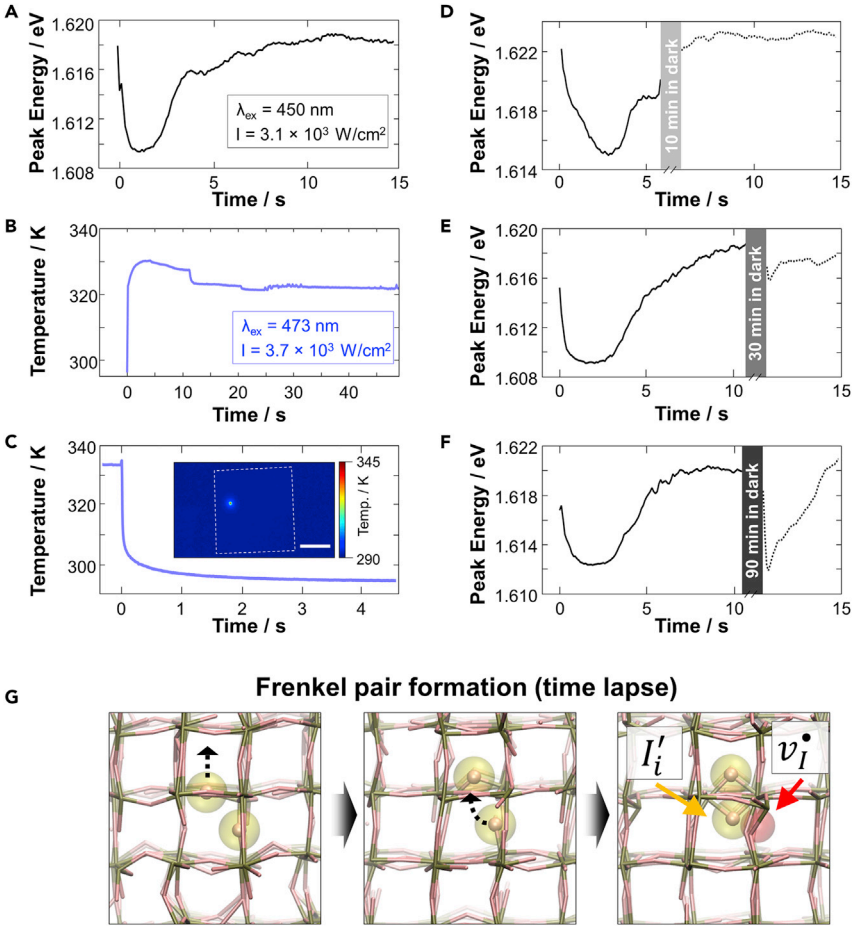

Figure 1. Ionic defect formation as a response to intense light

(A) Evolution of photoluminescence peaks of a $MAPbI_3$ thin film continuously illuminated with λ_{ex} = 450 nm (2.75 eV, 3.1 kW/cm^2) excitation over the course of 15 s.

(B) Thermal-imaging results tracking the temperature under comparable excitation conditions (λ_{ex} = 473 nm at 3.7 kW/cm^2) and similar timescales. Minor fluctuations are due to the laser power being unstable, although the gradual changes were confirmed not to be caused by the laser by measuring the power before and after the experiments.

(C) Film temperature in the excited spot stabilizing within a few seconds after reaching maximum temperature. The inset shows a thermal map of the 25 × 25 mm^2 perovskite film. Scale bar in the micrograph represents 1 cm.

(D–F) Evolution of the PL peaks similar to (A), where varying periods of rest in dark (10, 30, and 90 min, respectively) were introduced.

(G) Three snap shots from the *ab initio* molecular dynamics calculation showing the formation of an iodide Frenkel pair as a response to introducing excess thermal energy (800 K). One iodide atom moves beyond its designated location (top) spontaneously, which disrupts the ideal 180° Pb–I–Pb bond angle to accommodate a second iodide atom (middle), which results in the formation of an iodide interstitial and vacancy (bottom).

indications of emission from PbI_2 (Figure S2). We performed a heat-diffusion analysis using the experimental excitation conditions (Notes S1 and S2) to understand what temperature the film could be expected to reach via the release of excess photon energy above the band gap. For a single photon with energy 2.75 eV (λ_{ex} = 450 nm), the thermalization energy is in excess of 1 eV assuming a band gap of 1.56 eV. Our model shows that, due to the low thermal conductivity of halide perovskites,[14,15] the thermalization energy should, in the absence of any heat-dissipation

channels, warm up the illuminated volume of the film to ~600 K within a few milliseconds. This should result in a rapid degradation of the film in the illuminated spot,[16–18] and a corresponding change in the perovskite PL spectrum, which conflicts with our experimental observations.

To identify the origin of the unexpected photostability, we performed thermal-imaging measurements of the film under exposure with similar excitation conditions as the PL measurements (λ_{ex} = 473 nm at 3.7 kW/cm^2) and observed that the maximum temperature reached is approximately 330 K (Figure 1B). Moreover, the temperature stabilizes at a lower temperature after 15 s of illumination, which is an unexpectedly long time considering that the sample is subjected to a constant photon flux. The surprisingly low temperature of the illuminated spot of the film explains why no degradation is observed and why the PL emission remains perovskite-like[19] and confirms the inconvenient discrepancy between the measured and expected temperature of the film at such high photon fluxes. This suggests that some endothermic mechanism acts on the system and subtracts part of the photon thermalization energy beyond the heat diffusion accounted for by our model (see Note S3 for additional thermal-imaging results).

To identify this endothermic mechanism, we focus on PL data and screen possible photoinduced processes that give rise to the PL blue shifts and could potentially be driven by a temperature increase. Although not affected by temperature, we first rule out the Burstein-Moss effect[20] due to the relatively "slow" dynamics observed here for the evolution of the PL shift while the excitation is constant. Next we consider lattice expansion, which produces a PL blue shift when temperature rises.[11,21] We measured the temperature of the film after switching off excitation and observed that it reaches room temperature within a few seconds (Figure 1C), which is consistent with our heat-diffusion calculations (Note S2). If the PL shift is caused by lattice expansion, the PL peak should return to its initial position after the excitation is turned off within a similar time window as the temperature. We therefore repeated the measurements tracking the PL peak position and introduced a dark period once the PL peak had shifted (after 5–10 s). Thereafter, the illumination was turned back on, and the PL peak position was again tracked (Figures 1D–1F). Despite a 10-min rest period, which is far longer than the time required for the film to return to room temperature, the PL peak position upon switching the illumination on again, not only remained blue shifted, but essentially continued the same trend as if no dark period had occurred (dashed gray trace in Figure 1D). These observations render lattice expansion, as well as any mechanism relying on heat diffusion, ineligible for causing the observed PL blue shift.

When the dark period was extended to 30 min, a slight recovery of the peak is seen (Figure 1E), which is further emphasized by extending the dark period to 90 min, after which the recovery becomes obvious (Figure 1F). Recovery of the PL signal, as well as device-performance parameters, over several minutes to hours in dark after exposure to light have previously been related to the recovery of defects that likely formed during the light exposure.[3,22–24] The slow stabilization of the temperature, and the long timescales required to recover the PL peak position in dark, are both compatible with previously reported timescales of defects forming and migrating under light, as well as their ability to recover and restore optoelectronic properties.[23,25–27] Hence, we conclude that defect formation is likely the cause of the PL blue shift.

Another potential process that is both slow and triggered by heat is the tetragonal-to-cubic phase transition, which occurs at temperatures slightly higher than

the maximum temperature observed in our thermal-imaging measurements (~330 K).[28] Indeed, if the tetragonal-to-cubic and cubic-to-tetragonal are first-order phase transitions, the system might be kinetically trapped in the initial phase upon both heating and cooling (kinetic trapping in a metastable phase). However, there is no clear evidence in the literature that these are first-order phase transitions. Moreover, in Figure S1, we demonstrate that lower photon fluxes, which should translate into lower film temperatures, also yield a PL blue shift. We therefore rule out phase transition as an explanation for our observations.

To identify a process that can involve the formation of mobile ionic defects by indirect heating of the sample via thermalization of excess photon energy, we simulate a bulk $MAPbI_3$ structure supplied with a thermal energy equivalent of the excess energy produced in the experiment yielding the results in Figure 1A (see also Note S2). To account for the possible effects of the presence of charge carriers, we also simulate negatively and positively charged samples, modeling electrons in the conduction band and holes in the valence band, respectively. Interestingly, despite the injected high thermal energy, the system retains its perovskite structure; however, it spontaneously forms an iodide Frenkel pair (vacancy, $v_I^{\bullet}$, and interstitial, i_I'). The images shown in Figure 1G illustrate this process as observed in the neutral system; matching results have been obtained in the presence of simulated charge carriers. These simulations provide theoretical support that the excess thermal energy generated by the thermalization of hot carriers can lead to the formation of Frenkel defect pairs by the breakage of Pb–I bonds.

The PL blue shift via the formation of defects is a unique feature of halide perovskites, which is associated with the antibonding nature of the top the valence band. The formation of iodide and/or methylammonium Frenkel pairs induces a deformation in the inorganic sublattice which, in turn, reduces the antibonding negative overlap between 6s Pb and 5p I atomic orbitals forming the valence band maximum orbital. The reduction of the antibonding overlap results in a stabilization (i.e., reduction of energy) of valence frontier orbitals, which causes a widening of the band gap.[29] This mechanism is, indeed, consistent with theoretical reports on the trend of perovskite band gaps with distortion of the inorganic sublattice.[30] Defects distorting the lattice and causing a PL peak shift toward higher energies is both in good agreement with previous reports[19,30,31] and corroborated herein by theoretical calculations (Note S2). In Note S1, we extend the discussion with a detailed analysis of the PL peaks and intensities at different excitation power densities, confirming that the PL peak shift is not caused by a direct thermal effect, where extended measurements indicating prolonged photostability at intense fluxes are also shown.

Photoinduced ionic defect formation mechanisms

From the discussion above, we arrive at the conclusion that a mechanism involving the formation of defects must exist to efficiently dissipate enough excess energy to keep the film from detrimentally overheating. In other words, the excess energy of intense photon fluxes goes to forming defects instead of thermalizing and heating up the lattice. Thus, the formation of ionic defects acts as a direct line of defense against thermal decomposition from the absorbed excess photon energy. We emphasize that it is *not* the presence of defects but rather their formation that protects the $MAPbI_3$ film from degrading.

Since the mechanisms of forming defects by light depend on the excess absorbed energy above the band gap, we consider three scenarios of defect formation under illumination (Figure 2A): (1) the thermal pathway, where the excess energy from

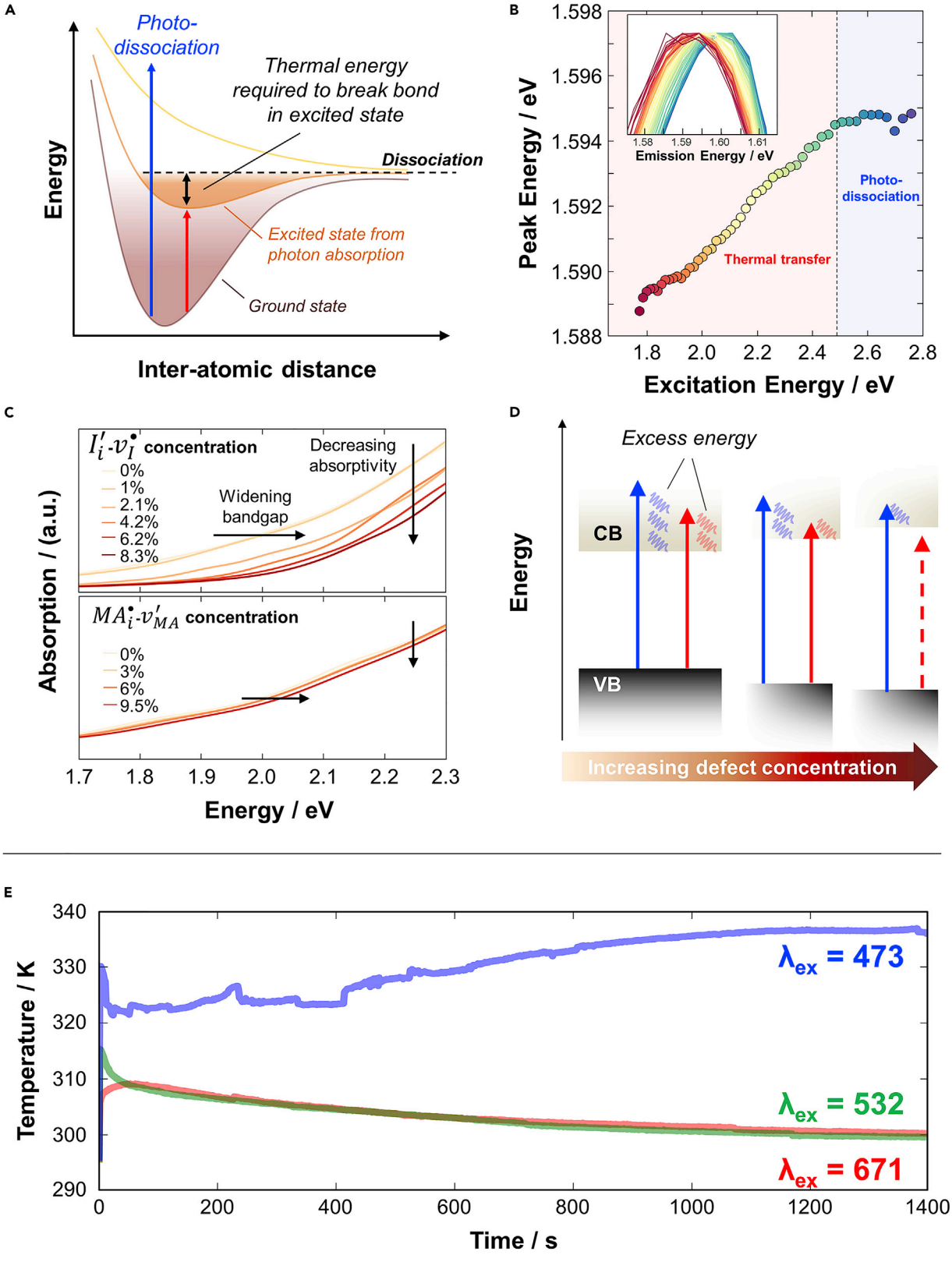
A
Photo-dissociation
Thermal energy required to break bond in excited state
Dissociation
Excited state from photon absorption
Ground state
Energy
Inter-atomic distance
B
Peak Energy / eV
Excitation Energy / eV
Emission Energy / eV
Photo-dissociation
Thermal transfer
C
I_i'-$v_I^{\bullet}$ concentration
0%
1%
2.1%
4.2%
6.2%
8.3%
Decreasing absorptivity
Widening bandgap
$MA_i^{\bullet}$-v_{MA}' concentration
0%
3%
6%
9.5%
Absorption / (a.u.)
Energy / eV
D
Excess energy
CB
VB
Energy
Increasing defect concentration
E
Temperature / K
Time / s
λ_{ex} = 473
λ_{ex} = 532
λ_{ex} = 671

Figure 2. Mechanisms of ionic defect formation

(A) Schematic showing the possible pathways via which bonds can break after photon absorption: photodissociation, via thermal energy, or a combination of both.

(B) Excitation energy dependence on the PL emissive peak position; inset shows the normalized emission peaks with the same color coding as the main panel. In the first regime, the peak blue shifts with a linear trend for increasing excitation photon energies until a threshold of ~2.5 eV is reached, after which in the second regime the peak shift remains rather stable (separated by a black dashed line). We attribute the former to defect formation dictated by thermal transfer of excess energy and the latter driven by photodissociation.

(C) DFT calculated absorption of a pristine $MAPbI_3$ lattice and lattices with different iodide and methylammonium Frenkel pair defect concentrations demonstrating both a shifting of the band gap as well as a reduction in absorptivity (black arrows).

(D) Schematic demonstrating the excess energy changing with an increasing band gap due to defect formation where lower photon energies eventually have minimal absorption.

(E) Temperature evolution over 20 min using three excitation wavelengths (λ_{ex} = 473 nm, blue; λ_{ex} = 532 nm, green; λ_{ex} = 671 nm, red).

photons with energies above the band gap is released into the lattice via hot carrier cooling, causing the dissociation reaction. (2)The photodissociative pathway, in which the absorbed photon energy is high enough to bring the system into a *dissociative state* and directly break one or more chemical bonds (e.g., between Pb and I) without any additional energetic barrier. Such a path is frequent in photochemical reactions of molecular systems.[32] For halide perovskites, the photodissociative pathway has been proposed to be the mechanism behind light-induced decomposition of PbI_2 into metallic lead (Pb^0), where the photons with sufficient energy directly break Pb-I bonds.[33,34] (3) The two previous mechanisms acting synergistically, where absorbed photons bring the system to a bound excited state and weaken chemical bonds so that they can be broken with less thermal energy.

With increasing excitation photon energy, scenario 1 should produce more defects directly related to the amount of excess energy that is generated. In contrast, for scenario 2, increasing the photon energy beyond the level required to induce photodissociation does not generate more defects in direct correlation with photon energy. To verify the proposed scenarios, we measured the PL peak position as a function of excitation wavelengths between 450 and 740 nm (2.67–1.67 eV), under the assumption that the extent of the PL blue shift reflects the light-triggered defect concentration (Note S4). A moderate fluence of ~1–2 suns was used, keeping the photon flux constant for all excitation wavelengths (Figure 2B). For excitation energies below 2.5 eV, an almost linear increase of the PL blue shift can be seen, which we relate to defects being generated primarily via a direct thermal pathway (scenario 1). This continuous dependence on the excited photon energies suggests that this mechanism is already active at low photon energies, which excludes, for example, deprotonation of MA as previously proposed[35] or any mechanism requiring high photon energies. For higher photon energies, the PL peak shift plateaus despite increasing excitation photon energy, suggesting that the defects are predominantly generated via photodissociation (scenario 2). Thus, the photon energy determines the pathway whereby energy is released into the system, which in turn may trigger different degradation processes. Several previous reports have demonstrated an excitation energy dependence on both PL signatures[36,37] and degradation mechanisms,[35] which may be tied to our hypothesis.

The formation of Frenkel defect pairs (e.g., of iodide and MA) can efficiently dissipate the excess energy via the thermal (scenario 1) or combined thermal and photodissociation (scenario 3) pathways, thus preventing the film from reaching very high temperatures and rapidly decomposing. The high dielectric constant of $MAPbI_3$ might help to stabilize the formed defects that store the excess energy[38–40] and thus prevent an immediate reinjection of the energy into the lattice. *Ab initio* calculations show that the excess thermal energy could result in the formation of a high concentration of iodide and methylammonium Frenkel pairs (Note S4). However,

the resulting imbalance of the concentration of defects in the hotspot and surrounding regions triggers their diffusion. This process would be assisted by the selective attraction of grain boundaries for charged defects.[23,40] Together with the relatively flat energy profile for Frenkel defect pair separation (Note S4), which favors the separation of defects of opposite charge, their immediate recombination to release energy back to the lattice is prevented. Consequently, the lattice temperature is kept low via a "defect energy buffer" despite a high photon flux.

The formation of defects as a response to extensive photon absorption cannot alone explain the resilience to permanent degradation under prolonged exposure at high intensity. We calculate the energy cost of forming different types of defects in $MAPbI_3$ (Table S1), where, for example, an MA Frenkel pair consumes around 1 eV. If we assume all excess energy goes into forming defects, our thermal model allows us to assess how much energy needs to be consumed at 30,000 suns in order to maintain a film temperature of 330 K. We find that the lattice corresponding to the volume illuminated by a Gaussian beam with a full width at half maximum (FWHM) of 6 μm, would saturate with defects within microseconds, completely degrading the film. Even reducing the percentage of absorbed energy that goes into forming defects to 1% cannot explain our observations. Thus, the process of forming a defect in response to photon absorption is clearly insufficient to explain the observed stability.

To understand the missing link, we used density functional theory (DFT) to compute the absorption spectrum of the material as a function of defect concentration (iodide and methylammonium Frenkel pairs) and found that the perovskite band gap widens with increasing defect concentration, which aligns with our hypothesis regarding the origin of the PL blue shift above. In addition, the absorptivity at higher energies also is reduced. These trends are shown in Figure 2C (black arrows) for both iodide and MA Frenkel pairs. Here, due to the limited size of computational samples for DFT calculations, we considered only the case of relatively high defect concentrations. However, even with a lower defect concentration, molecular dynamic simulations[41] in combination with DFT calculations show that the Frenkel defects influence the structure of perovskites, namely the off-centering of Pb,[42] which indirectly causes the band gap to increase (Note S4; Figure S9).

The dependence of the absorption spectrum on defect concentration becomes critical as it provides a necessary step to help rationalize a mechanism that balances the energy absorbed, and energy dissipated in the perovskite lattice. Widening of the band gap and reducing absorptivity over a broad spectral range with increasing defect concentration reduces the available energy left to thermalize after absorption, which in turn lowers the potential to form additional defects (see schematic in Figure 2D). Moreover, as the defects recombine at a far slower rate than they form—and likely at a location outside the illuminated region due to diffusion—the energy is gradually released into the lattice, which effectively reduces the lattice thermal impact. Overall, the combination of these effects, together with an increasing defect formation energy with higher defect concentration (Note S4; Table S1), culminates in a self-regulating defect formation mechanism acting to prevent $MAPbI_3$ from irreversible degradation when exposed to light of increasing fluxes.

We tested our hypothesis by extending the thermal-imaging measurements to 20 min of continuous exposure to light at three excitation wavelengths (473, 532, and 671 nm, hereafter referred to as blue, green, and red respectively) at

an intense flux of ~30,000 suns (Figure 2E). Shortly after the light is turned on, the temperature increases for all excitation wavelengths. Over the entire measurement period, the temperature at all three excitation wavelengths gradually stabilizes, although for blue, the temperature initially increases, which is in contrast to red and green where a stationary temperature lower than the initial maximum is reached. We find these results consistent with our hypothesis of the photon energy dependencies of the different defect formation pathways; green and red light generate defects via thermalization (scenario 1) and blue via photodissociation (scenario 2).

Structural investigation

PL microscopy can provide detailed information on the photophysical changes induced on the perovskite electronic structure by light, but it requires intense irradiation due to the comparatively low sensitivity provided by such experiments. To demonstrate that similar processes also occur at moderate and device-relevant photon fluxes, we conducted *in situ* synchrotron wide-angle X-ray scattering (WAXS) measurements in transmission geometry under high vacuum using a four-crystal monochromator beamline[43,44] (Note S5) to monitor light-induced structural changes in the material with high sensitivity. For light excitation, an LED source (450 nm/2.76 eV, 50 mW/cm^2) was used.

Figure 3 shows the evolution of the 1D WAXS patterns over time. We confirmed that the synchrotron radiation only had minimal effects on the perovskite structure during 30 min prior to turning the excitation light on (Note S5). During illumination, a slight yet notable change occurs in the 004 and 220 reflections as can be seen in the heatmap in Figure 3A. As the light is turned off, the reflections do not return to their initial positions, as would be expected if the changes in the structure would be purely due to thermal effects, but rather continue to contract over the following 30 min (Figure 3A). After 30 min in the dark, an additional reflection appears between the 004 and 220 reflections (Figure 3B), which is indicative of the 200 reflection from cubic domains (details of lattice parameters change can be found Note S5). Rather than a light-triggered, thermally induced phase transition, which was excluded as an explanation for the PL blue shift where the photon flux was orders of magnitude higher than what is used in this WAXS experiment, we propose that the appearance of this peak is caused by a structural change relating to the formation of defects. As both I-related and MA-related Frenkel defect pairs form, the physical restraints associated with the *I*4/*mcm* octahedral distortions are diminished. Over the whole material, this would allow the Pb–I–Pb angle to approach 180° in all crystal directions (between the PbI_6^{4-} octahedra) resulting in the material adopting a more isotropic structure that ultimately has higher symmetry. This could result in similar reflections to the $MAPbI_3$ cubic structure shown in Figure 3B.

After illumination, the ionic defects may recombine and form volatile products, such as I_2 vapors or MA-related compounds,[2,33] which are quickly removed by the vacuum (discussed further in Note S5). We note that this latter process is absent in the other measurements, which explains why the material cannot recover in dark during the WAXS experiment, as observed during the PL measurements (Figure 1A). We stress, however, that the WAXS data provides evidence for an abrupt structural change under illumination, which indicates that the light-triggered defect formation also occurs at a *moderate light intensity*. Hence, the proposed mechanism is also relevant for devices at common operating conditions.

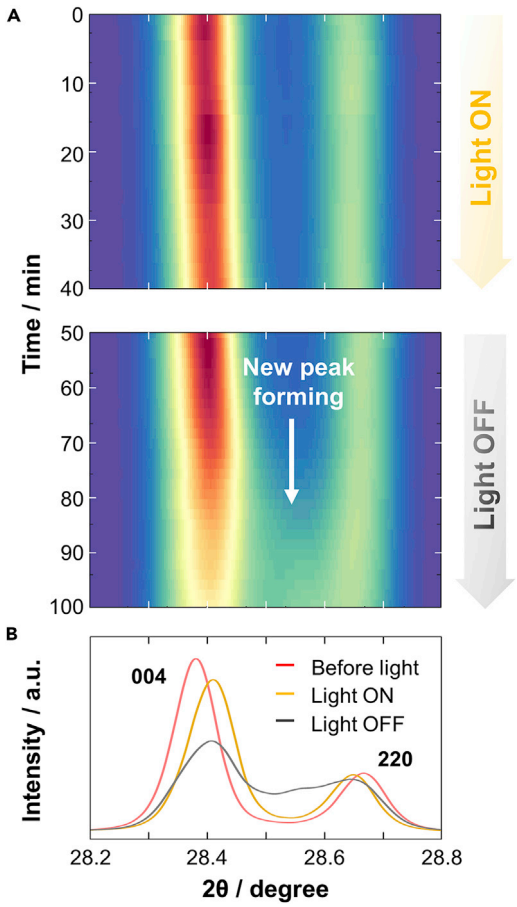

Figure 3. Structural response to ionic defect formation

In situ wide-angle synchrotron X-ray scattering measurement at a photon energy of 8 keV with blue light excitation of the sample.

(A) Heatmap of time evolution focusing on 004/220 reflections.

(B) 1D line extracted before illumination (red trace), at the end of the light excitation period (yellow trace), and at the end of the dark rest period (black trace) of the same region.

Recovery of defects in dark

While WAXS provides detailed insight into the light-related structural changes in the material, complementary techniques are required for spectroscopic insight into the mechanism. Raman spectroscopy is suitable to assess which ionic species are involved by identifying specific molecular vibrational modes.[28] We measured Raman spectra using a focused CW laser source with an emission wavelength at 532 nm (2.3 eV), to avoid triggering direct photodissociation (Figure 2B), while remaining far from the expected PL emission at 1.6 eV. A comparatively low photon flux of roughly 1.50 kW/cm^2 was used to acquire several baseline spectra confirming no significant change in the material composition (one example is shown in the top row of Figure 4 and the rest in Figure S14). The excitation density was increased to 750 kW/cm^2 for 10 s to induce degradation (see Note S6 for further details). Spectra were measured immediately after intense exposure and intermittently during a resting period in dark for 30 min at lower fluxes (bottom four panels in Figure 4).

The Raman spectrum of $MAPbI_3$ is characterized by a series of peaks, of which those in the range between 50 and 100 cm^{-1} can be assigned to the inorganic Pb–I framework, while those at 250, 350 cm^{-1}, and between 850 and 1,000 cm^{-1} are assigned

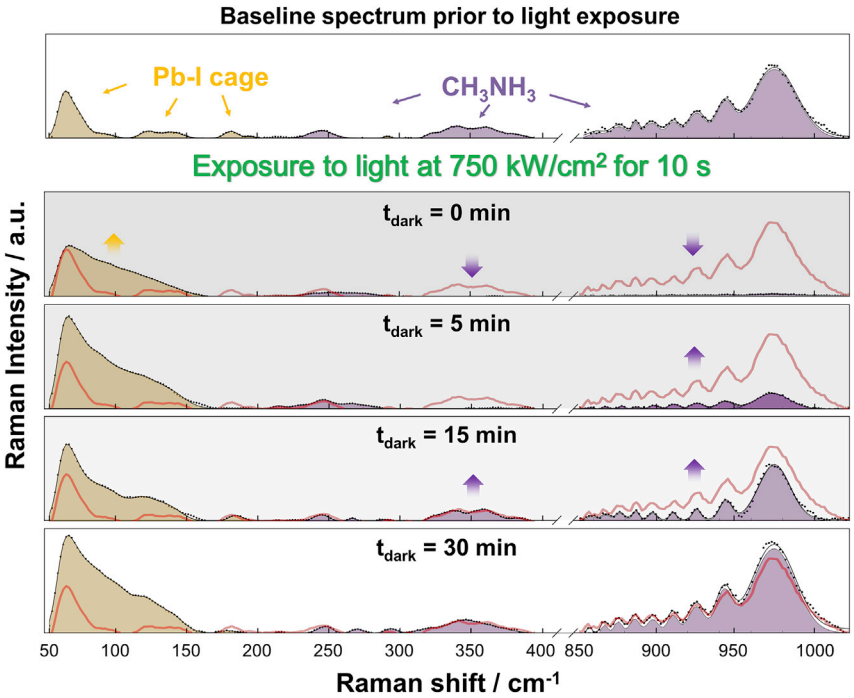

Figure 4. Dark recovery and the role of different ionic defects

Raman spectra measured prior to intense irradiation, directly after, t_{dark} = 0 min, and at various rest period in the dark—5, 15, and 30 min. The peaks around 350 cm^{-1} relating to the rotation of CH_3 with respect to NH_3 are unique for the MA cation[28] and disappear after irradiation with intense light, after which it recovers when given time to rest in the dark. Baseline corrected data are shown with black dots, and fits using multiple Gaussian line shapes are shown in solid black lines The red traces in the bottom panels act as a reference for the baseline spectrum. The measurement is performed at 193 K in an inert atmosphere to improve the signal to noise ratio. Although the appearance cluster of peaks observed at high frequency are not purely representative of individual vibration modes of MA, the emphasis is placed on the loss and subsequent restoration of these peaks as an indicator of MA recovery.

to internal modes of MA^+.[28,45–47] After intense exposure, the simultaneous decrease of the high-frequency peaks and increase of the low-frequency peaks indicate a loss of MA, which in turn affects the Pb-I cage structure, confirming the light-related structural reordering observed with WAXS. We note that the Raman spectrum collected immediately after intense illumination in Figure 4 (t_{dark} = 0 min) differs from the Raman spectrum measured on the film after fully degrading to PbI_2 (Note S6; Figure S15), further implying that the material is in a disordered phase with a high concentration of defects rather than pure PbI_2. This is corroborated by molecular dynamics calculations, which confirm that the defects formed in the structure can severely distort the perovskite structure, leading to changes in the vibrational spectrum similar to those observed experimentally (Note S6; Figure S16). We also subjected cesium-formamidinium (CsFA) lead iodide perovskite to the Raman measurement. As expected from a more stable perovskite, the CsFA perovskite could withstand a photon flux corresponding to nearly 5 million suns without degrading to PbI_2 (Note S6; Figure S18). This indicates that the ability to withstand intense illumination is not limited to $MAPbI_3$ and suggests that our findings can be relevant to other perovskite compounds as well.

After 30 min of dark rest, the Raman spectrum nearly completely recovered (t = 30 min; Figure 4), supporting existing literature showing that defects in

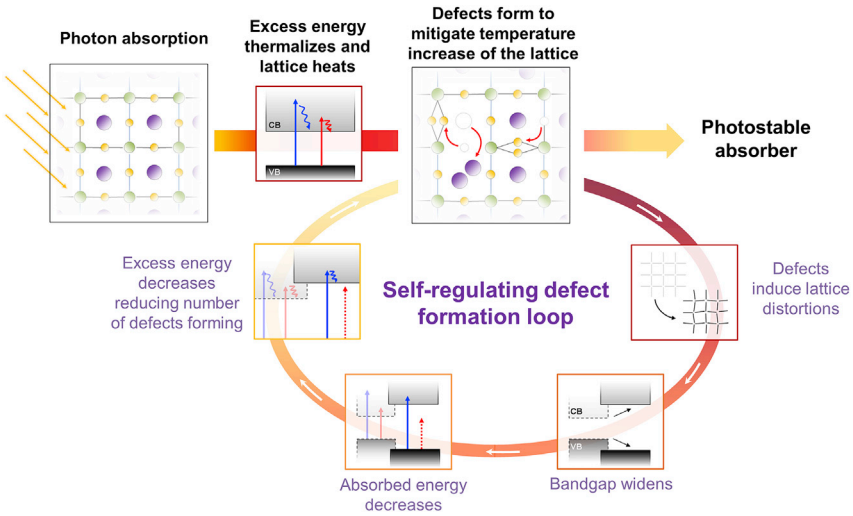

Figure 5. The photoprotection mechanism in halide perovskites

Schematic demonstrating the proposed photoprotection mechanism in $MAPbI_3$ thin films.

perovskite recover in the dark.[3,23,25] Here, we can tentatively relate this recovery to the organic cation returning to its A-site position in the $MAPbI_3$ structure, which has been previously proposed,[25] although it has not been experimentally demonstrated as specifically as herein. Similar to a previous study of ours, we demonstrate with scanning electron microscopy-energy dispersive X-ray spectroscopy (SEM-EDX) that, upon intense illumination, the film exhibits a change in ionic distribution, where a noticeable reduction of iodide and slight reduction of carbon signal (related to MA) can be observed in the illuminated region. After a period of dark rest, we observe a recovery of both iodide and carbon signals (Note S7). Figure 4 further relates the recovery of $MAPbI_3$ after illumination to ionic defect recovery likely involving MA^+ ions.

We note that the Raman signal between 70 and 100 cm^{-1} relating to the inorganic framework increased after recovery, indicating a crystallinity enhancement. This observation coincides with an increase in the relative PL yield measured during the Raman experiment (Figure S17). We attribute this to a slight reordering of the structure during recovery, leading to improved optoelectronic properties of the absorber. However, we also acknowledge that this increase in intensity can be related to polyiodide released from the sample after intense illumination,[48] which is a promising direction for further investigations.

Photoprotection in halide perovskites

Based on the results presented up until this point, we propose an inherent photoprotection mechanism of $MAPbI_3$ perovskites centered around the critical ability of the material to promptly form defects when exposed to light. In this mechanism (Figure 5), the formation of defects results in resilience against photodegradation in two ways: (1) on the short timescale, defect formation mitigates the release of excess energy into the lattice, which limits the film temperature; and (2) on the long timescale, the widening of the band gap reduces the absorbed photon energy available to drive any degradation process. In combination with the light-trigged defects being able to gradually recover, this creates a possibility for the absorber to retain its operational stability over a longer period. The process of forming a defect (and *not* the presence defects themselves) removes the excess thermal energy that would otherwise rapidly dissipate into the lattice causing a high thermal impact and

consequently prevents complete degradation of the film upon intense illumination exposure. Additionally, an essential aspect of the photoprotection mechanism is the self-regulating nature, in which photon absorption is reduced as a function of increasing defect concentration due to a distorted, yet structurally intact, perovskite phase.

We tested the long-term stability implied by the photoprotection mechanism by illuminating a $MAPbI_3$ thin film with 300 suns ($\lambda = 637$ nm; 1.9 eV) for 5 h. After exposure, grazing-incidence WAXS (GIWAXS) measurements reveals a modest amount of PbI_2 in the exposed region, while the relative strength of the $MAPbI_3$ reflection peaks suggests the majority of the interrogated volume is still perovskite (Note S5; Figure S13). Moreover, comparing PL spectra within and outside the exposed region, no essential changes can be seen.

The extended thermal-imaging measurements (Figure 2E) showed a gradual stabilization of the temperature, which is consistent with the photoprotection mechanism balancing the formation and recovery of defects with the incident flux. Without the photoprotection mechanism regulating the absorbed energy via defect formation, we calculate that the film would need to consume up toward 10^4 J of excess photon energy without degrading, which is inconceivable.

Prolonged exposure to light produces a constant surplus of defects, and it becomes necessary to provide an extended period in the dark to restore the optoelectronic properties of the film. This notion aligns well with several reports on the improved long-term stability of perovskite-based devices given a substantial period to recover in the dark.[3,49] Now, being able to relate this stability to the formation of defects, and having shown its dependence on photon energy (Figure 2; see also Note S7), we confirm the recovery of open-circuit voltage (V_{OC}) (which relates to defects) in $MAPbI_3$-based solar cells during diurnal cycling when subjected to different photon energies (see Note S9). In short, a high photon energy (greater than the PbI_2 band gap) leads to photodissociation to Pb^0, which accumulates and prevents device recovery. On the contrary, long-term photostability can be enhanced with devices subjected to low photon energy because of the formation and recovery of defects with day/night cycling. This provides fundamental insight into the device recovery reported in the literature, where a fluctuating V_{OC} is often reported.[3,4,49]

The proposed photoprotection mechanism in halide perovskites also suggests that this material is suitable for applications involving exposure to intense irradiation, such as solar concentration PV. To explore this, we recorded the performance of a $MAPbI_3$ p-i-n solar cell with maximum power point (MPP) tracking under continuous illumination. We compare the device's performance under 1 sun and 5.5 suns (see supplemental experimental procedures for experimental details and calibration of photon flux). Figure 6 shows the 1-sun stabilized efficiency at 16.4%, after which a relative boost of 6.7% toward 17.5% of the efficiency is obtained at 5.5 suns. This is in agreement with the theoretical prediction by Lin et al.,[50] as well as their experimental demonstration.[51] The fact that a perovskite device can withstand 5.5 suns with negligible degradation while the bare absorber resists irradiation several orders of magnitude higher implies that perovskites can be a promising candidate for the next generation of concentration PVs. An extended MPP tracking can be found in Figure S8 (see also Note S8), which shows that the perovskite device retains more than 98% of its initial efficiency after 18 h of continuous tracking at 3 suns. Here, we used a larger Fresnel lens that reduces the flux but increases the area, allowing us generate data over many pixels to acquire an average. To realize

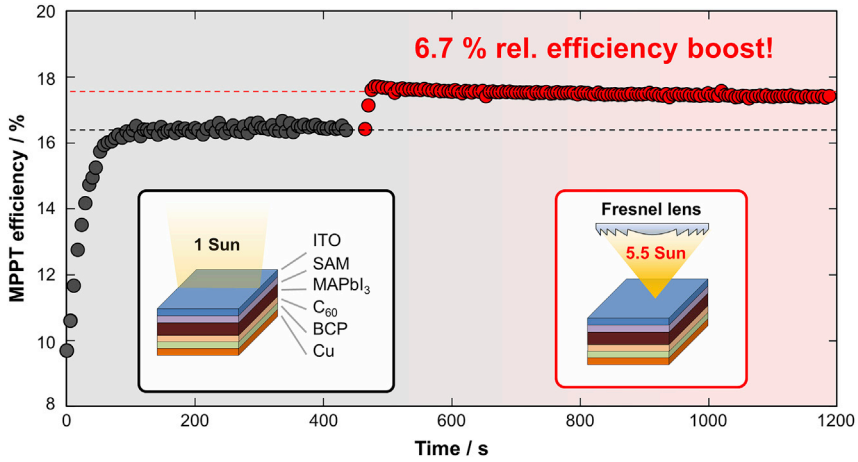

Figure 6. Stability and improved efficiency under concentrated sunlight

MPP tracking at 1 sun (black dots) and 5.5 suns (red dots) of a $MAPbI_3$ device. The concentrated sunlight is obtained by inserting a Fresnel lens. Both fluxes are calibrated using a silicon reference after which the plotted traces are normalized accordingly (see Note S8 and supplemental experimental procedures for further details on devices and measurement procedure).

perovskite-based concentration PV, our result suggests that the focus should be shifted toward the development of the contact and transport layers, and general device design that can withstand high photon fluxes rather than the intrinsic photostability of the absorber under such conditions.

While new standards for testing device stability have been proposed involving diurnal cycling of simulated sunlight,[49] our findings imply that heat-stress testing alone, as suggested by the IEC 61215 protocol, may also have to be reconsidered as an assessment of perovskite stability. Our findings help rationalize why energy, either injected into the absorber directly via a thermal contact or indirectly through photon absorption and thermal relaxation, creates two widely different scenarios. Without a thermal protection mechanism, the perovskite becomes unstable when direct heat is applied. Under illumination, the excess photon energy above the band gap is provided with an alternative relaxation pathway by forming defects in the optically excited system, which is critical for photostability.

There are certainly limits to which a film under illumination can remain resilient against permanent degradation, which we have to some extent demonstrated depending on a combination of photon flux and photon energy. Additionally, the initial material properties should also dictate the range under which the photoprotection mechanism can efficiently operate, where properties such as the number of grain boundaries and the initial defect concentration likely play an important role. These may affect the rate at which ionic defects can form, migrate, and recombine, which then become parameters that in our model determine the fluxes under which prolonged stability can be obtained. The picture certainly grows increasingly complex when adding transport layers and contacts to the absorber in a full device. This work therefore serves as an introduction to a novel concept that provides new insight into how photostability should be viewed in metal halide perovskites.

Photoprotection as an inherent mechanism may be a new concept for semiconductors; however, it is a well-known feature of many natural photosynthetic systems that have developed various mechanisms to mitigate excess energy from intense and/or

prolonged irradiation to maintain long-term efficient photosynthesis.[52] Without these mechanisms, life-sustaining vegetation would in some cases permanently degrade after only minutes of exposure to direct sunlight.[53] Photosynthetic photoprotection mechanisms are also self-regulating as nature has found several ways to dissipate excess energy under a range of incident solar fluxes, with a reaction time to alternating light intensities on a timescale of minutes.[8] Thus, it is promising that photoprotection via a self-regulating mechanism, which evidently is a critical feature of natural light-harvesting systems, is also found in halide perovskites. If a parallel can be drawn to photoprotection in plants, our results suggest that the interplay between defect formation and defect recovery are key processes leading to improved resilience against degradation of the perovskite absorber under intense illumination for extended periods of time. While these processes have separately been studied extensively, our work sheds new light on how the two processes operating together, and their impact on the optoelectronic processes, could improve photostability in halide perovskites.

Conclusion

We have presented a detailed study combining several *in situ* experiments and theoretical techniques to illuminate the mechanisms behind the unexpected photostability of halide perovskites, focusing on defect formation, defect recovery, and how they relate to photon energy and flux. We have demonstrated the resilience of $MAPbI_3$ thin films to intense photon fluxes up to several tens of thousands suns. We described the mechanism by which this is made possible via the formation of ionic defects based on thermal and photodissociation processes, which are dependent on the incident photon energies. Defects form in response to absorbed excess energy, which would otherwise thermalize via hot carrier cooling. This behavior reduces the thermal energy supplied to the system protecting it from irreversible thermal decomposition. We, therefore, demonstrate that the formation of defects serves a crucial purpose for photostability in halide perovskites, which could impact future strategies in compositional engineering. However, further experimentation is needed comparing two compositionally different perovskites, where one is particularly engineered to be photo stable, in order to determine whether such efforts are counterproductive toward photostability. Moreover, resilience to a high photon flux during operation, coupled with the ability of defects to recover when resting in the dark, naturally makes this intriguing material even more attractive for energy applications, such as concentration photovoltaics.

EXPERIMENTAL PROCEDURES

Resource availability

Lead contact

Further information and requests for resources and materials should be directed to and will be fulfilled by the lead contact, Aboma Merdasa (aboma.merdasa@med.lu.se).

Materials availability

This study did not generate new unique materials.

Data and code availability

This study did not generate any unique datasets or code.

Perovskite thin-film fabrication

The glass substrates were cleaned with soap (2% Mucasol in deionized water), acetone, and isopropanol in an ultrasonicator for 15 min. Then the substrates

were treated with UV–O_3 for 15 min prior to perovskite fabrication. After UV–O_3 treatment, the substrates were immediately transferred to an N_2 filled glovebox.

The methylammonium lead iodide perovskite solution consisted of 1.2 M solution of MAI:PbI_2 with 1:1 stoichiometry in mixed DMF:DMSO (v:v 6:1) (Sigma Aldrich). The methylammonium iodide was purchased from Dyenamo and lead iodide was purchased from Tokyo Chemical Industry. The solution was put in thermo shaker at 60 degree for 5 min to ensure full dissolution.

The triple cation CsFAMA perovskite is prepared as detailed described in Ref. [54]In short, the MAFA solutions were from 1.5 M PbI_2 and $PbBr_2$ (TCI) stock solutions in DMF:DMSO (v:v 4:1) (Sigma Aldrich) mixing with formamidinium iodide and methylammonium bromide (Dyenamo) to have mixed perovskite solution of 1.24 M with the ratio of 83:17 (FA:MA) by volume. The final 5% of Cs was added from CsI (abcr GmbH) (1.5 M in DMSO, Signma Aldrich). All chemicals were used as received.

Solar cells fabrication

Indium tin oxide (ITO) substrates (Automatic Research, 15 $\Omega \cdot cm^{-2}$) were cleaned as mentioned above. Prior to perovskite deposition, PTAA (poly[bis(4-phenyl)(2,4,6-trimethylphenyl)amine]) (Sigma Aldrich) with a concentration of 2 mg/mL in toluene (Sigma Aldrich) was spin-coated on clean substrates (4,000 rpm for 30 s). For the self-assembled monolayer (SAM), 100 μm from 1 mM solution of either MeO-2PACz or 2PACz (TCI) in anhydrous ethanol (Sigma Aldrich) was spun on top of the substrate. The substrates were then annealed at 100°C for 10 min to remove residual solvents. More details of the deposition and the molecules can be found in Al-Ashouri et al.[55] 100 μL of perovskite solution (prepared as mentioned above) was dropped on a room temperature substrate before starting the spin-coating program (4,000 rpm for 30 s, ramping for 5 s). After 20 s of spin coating (after 25 s for CsFAMA), 500 μL of ethyl acetate was dropped on the substrate to form a smooth and compact film. The perovskite film was immediately annealed at 100°C for 60 min. For the devices used in concentrated sunlight, the perovskite was made as previously reported.[56] In short, $MAPbI_3$ layer was fabricated using slot-die coating method using the 2-methoxy-ethanol (2-ME) based ink with dimethyl-sulfoxide (DMSO) as an additive. Finally, C60 (20 nm) (Sigma Aldrich), BCP (bathocuproine or 2,9-dimethyl-4,7-diphenyl-1) (10 nm) (Sigma Aldrich), and Cu (100 nm) (Alfa Aesar, 99.95% purity) were evaporated on the perovskite layer to complete the device. All of these fabrication steps were done in an inert atmosphere with minimal air exposure. All chemicals were used as received.

Scanning electron microscope and energy dispersive X-ray

The SEM images and EDX mapping were collected with Hitachi S4100 at 30k× magnification. The voltages used for SEM and EDX were 5 and 12.5 keV respectively.

Current density-voltage measurement

The J-V measurement was done with 1 equiv sun illumination from an Oriel LCS-100 class ABB solar simulator in an inert atmosphere with a cooling copper block set temperature at 23°C degree, which gave an estimated cell temperature of 25°C under one sun illumination. The device's active area was 0.16 cm^2 defined as the overlapping area between the metal electrode and the pattern of ITO substrate. The lamp was calibrated with a silicon 1 cm^2 diode certified by Fraunhofer ISE.

Photoluminescence microscopy

The measurement was performed in a homebuilt upright microscope. For excitation, we employed either a 450 nm diode laser (Thorlabs, CPS450), 637 nm diode laser (Thorlabs, HL6388MG), or 470 nm LED (Thorlabs, M470F3), which were all reflected into main the optical path using a dichroic mirror with a cut-on wavelength at either 500 or 625 nm depending on the excitation wavelength. The excitation was focused onto the sample via an objective (Nikon CFI-60 ELWD). Additional interference filters were used to filter out the excitation after the back side of the dichroic mirror. At the intermediate image plane, a variable slit was placed to only allow a vertical line of the image to pass to the detector. A relay lens system was used to image the intermediate plane at the position of the camera (Thorlabs, CS505MU). Prior to the camera, a transmission grating (Thorlabs, GT25-06V) was placed to disperse the photoluminescence (PL) passing through the slit onto different parts of the camera sensor depending on photon energy. This allowed simultaneous extraction of complete PL spectra at every location along the slit with a time resolution of 50 ms. For the excitation dependence measurements (Figure 2), a supercontinuum light source (NKT Photonics, SuperK Extreme) was used in another custom configuration as described in reference.[37]

Thermal imaging

The measurements were performed using a thermal camera from Teledyne FLIR (model A655SC) with a 640 × 480 microbolometer sensor capable of detecting temperature differences down to 30 mK. Measurements were made at a full frame rate of 200 Hz when measuring dynamics over a few seconds, and a frame rate of 6 Hz when measuring dynamics over a period of several minutes. The sensor was placed at a distance of roughly 20 cm from the target, which was suspended vertically in the air using scotch tape at the edges in order to minimize thermal coupling to other objects. The effective pixel size was determined to be 24 × 24 μm^2. The laser was focused onto the film surface using a 40× microscope objective through the glass substrate. The thermal camera was placed on the opposite side of the film and shifted slightly off the optical axis to avoid direct exposure from the laser. This configuration was considered optimal since imaging through the objective was not an option due to lack of sensitivity in the spectral range between 7–14 μm. Imaging from the side of the objective was neither possible since the working distance of the objective was only a few mm. While focusing the laser through the 1 mm thick glass substrate introduces some uncertainty in estimation of the spot size, it provides the best opportunity for acquiring thermal images with the best focus of the perovskite film.

Wide-angle X-ray scattering

WAXS data were acquired at the four-crystal monochromator beamline of the PTB (Physikalisch-Technische Bundesanstalt) at the BESSY II synchrotron radiation facility (Helmholtz-Zentrum Berlin).[43] The *in situ* measurement used 8 keV photon energy (λ = 1.5498 Å) in a transmission geometry under high vacuum (10^{-7} mbar). The photon flux from the synchrotron beam, as measured with a photodiode, was 1.8 × 10^8 photons s^{-1} or 2.42 × 10^9 photons s^{-1} mm^{-2} (~0.31 mW/cm^2) over the oval-shaped beam spot with a height of 80 μm and a width of 300 μm, and the total beam exposure for the experiment was 5,600 s. Scattered X-rays were detected with a vacuum-compatible version of the PILATUS3 X 100K hybrid photon-counting detector (DECTRIS),[44] which rotated around the sample center in 4.5° steps through 10 positions at a sample-to-detector distance of 206 mm with 10 s of acquisition at each detector angle. These single images are azimuthally integrated and

combined to create the full diffraction pattern, using LaB6 as a calibrant. Data were analyzed and corrected using PyFAI.[57]

In the *in situ* synchrotron WAXS measurement, a 50 mW/cm^2 power density excitation with blue light (λ_{ex} = 470 nm, 2.76 eV—Thorlabs M470F3, 21.8 mW) was used. The external excitation light was focused through a glass window of the vacuum sample chamber onto the sample, the light source was mounted so that the light was transmitted through a window at 45° compared with the sample plane. An X-ray fluorescent crystal window (YAG:Ce 100 μm, Crytur) was used to determine that the synchrotron beam spot and the light excitation was overlapped with the synchrotron beam position. Note that the light intensity was estimated by focusing the light to 30 cm point in ambient conditions, which was similar to the distance between the light source and the sample in the experimental setup. However, due to the chamber window the light intensity might change due to a small difference in focal length. Samples were prepared with an X-ray transmissive stack of polyimide (8 μm)/$MAPbI_3$/PMMA (20 nm) following the same perovskite fabrication protocol detailed above.

Theoretical calculations

Ab initio simulations, both molecular dynamics (MD) and electronic structure calculations have been used to investigate (1) the nature of defects that are more likely induced by the thermalization energy injected in the system in absence and presence of charge carriers and (2) the energetics of various kinds of Frenkel pairs at several vacancy-interstitial distances.

Computational samples typically consist of 384 or 768 atoms, 32 or 64 stoichiometric units, obtained by replicating the unit cell of the tetragonal or cubic $MAPbI_3$ phases. Samples of analogous size have successfully been used before to study the physics of defects in metal halide perovskites.[58] All calculations were performed within the Perdew–Burke–Ernzerhof (PBE)[59] generalized gradient approximation (GGA) to the DFT. In principle, in halide perovskites, one expects a significant spin–orbital coupling (SOC). However, it has already been shown that SOC has little effect on the forces acting on nuclei and, due to an error cancellation, GGA is able to reproduce very well the band gap of lead halide perovskites.[60] In addition, van der Waals interactions might have an effect on the properties of the system. However, recent reports have shown that these effects on structural, vibrational, and electronic properties of hybrid perovskites are relatively minor.[61] Thus, we chose to use the GGA–DFT, which is computationally more efficient and compatible with the extensive MD simulations on a relatively large number of big samples. The reliability of this approach has been validated for specific cases, taking as reference the non-local vdW-DF2 functional.[62] It is worth remarking that this setup is consistent with computational approaches used in the recent literature.[63]

Rappe, Rabe, Kaxiras, Joannopoulos ultrasoft pseudopotentials[64] were employed to describe the interaction between valence electrons and nuclei plus core electrons. Kohn-Sham orbitals were expanded on a plane wave basis set with a cut-off of 40 Ry. Calculations concerning geometry optimization, cell relaxation and band structure calculations were performed with a 2 × 2 × 1 Monkhorst-Pack k-point sampling.[65] For computing spectra, we used a finer grid, 4 × 4 × 2. Finally, MD simulations were performed within the Γ-point approximation.

To identify the effect of thermalization energy on $MAPbI_3$ samples, we ran *ab initio* MD simulations at several temperatures (400, 600, and 800 K) for neutral and

charged samples, with +1 and −1 charge mimicking the presence of holes in the valence band and electrons in the conduction band, respectively. In all cases, at 800 K we observed the formation of Frenkel pairs within few picoseconds. Due to the small size of the sample, the Frenkel pairs could not split, and the defects eventually recombined.

The energy of formation of Frenkel pairs was computed by the difference of the average total energy of samples with and without Frenkel pairs, as obtained from *ab initio* MD simulations at 300 K: $\Delta E_{FP} = \langle E_{FP} \rangle_{300K} - \langle E_{Bulk} \rangle_{300K}$, where $\bullet_{300K}$ denotes the ensemble average at 300 K, as estimated by the time average along MD, E_{FP} and E_{Bulk} are the (instantaneous) energies of samples containing a Frenkel pair and without defect, respectively. In particular, here we considered Frenkel pairs at different initial relative positions, as illustrated in Note S9. Recent works have shown that, due to the soft nature of metal halide perovskites, it is crucial to take into account finite temperature effects in the formation energy of defects in this material.[58,66] Each simulation lasted ~10 ps during which neither vacancies nor interstitial defects forming the Frenkel pairs migrates from their original positions. Hence, present MD results were suitable to estimate the energy of a Frenkel pair as a function of the distance of the complementary defects within the range allowed by the computational samples. We also computed the energy of complementary defects at large distance (infinite separation) by separately computing the formation energy of a vacancy and an interstitial. Here, we considered defects in their *natural* charge state, e.g., positive for V_I and negative for I_I. In this case, finite size corrections for charged defects have been taken into account following Ref. [67]Optical (absorption) spectra were obtained from the dielectric function computed on samples containing defects at various concentration after their complete relaxation.

All aforementioned calculations were performed using the Quantum-Espresso suite of codes.[68]

MD simulations were based on a classical model potential for hybrid perovskites (MYP) force-field developped by Mattoni et al.[41] The model consists of a combination of Buckingham–Coulomb interactions for inorganic atoms and GAFF[69] for molecules. MYP is able to reproduce satisfactorily the structural, elastic, thermal,[70] and vibrational properties[71] of the different crystal structures of hybrid perovskites. Simulations were performed by using the large-scale atomic/molecular massively parallel simulator (LAMMPS) code[72] with hybrid style (lj/charmm/coul/long and buck/coul/long) and a cut-off as large as 10 Å. The long-range electrostatic interactions in triclinic cells were calculated by the Ewald sums method with a relative accuracy of 10^{-6}. Constant-temperature, constant-pressure ensemble (NPT) simulations were performed with a triclinic fully flexible simulation cell. A time step as small as 0.5 fs has been used to properly integrate equations of motions.

Defected systems containing interstitials, vacancies and Frenkel pairs were generated by inserting randomly the corresponding number of defects (ranging within 1–100) in an equilibrated perfect crystal of 256 formula units. The defects were distributed randomly with the constraint of avoiding the insertion of more than one defect per Pb–I octahedra. At each defect concentration and for each kind of defect the systems were characterized in terms of the volume and corresponding pseudo-cubic lattice parameter. Furthermore, the Pb off-centering was obtained by calculating, for each PbI_6^{4-} octahedra, the displacement of Pb atoms with respect to the center of mass of the neighboring iodine atoms. The continuous probability

$P(r_{off})$ of different r_{off} values was obtained by a Gaussian convolution of the discrete calculated values.

In order to get information on the vibrational properties of the system containing defects, the total and projected vibrational density of states were calculated. The mass-weighted atomic velocities ($m_a{}^{1/2}v_{a,i}$, where a,i are atoms and Cartesian coordinates, respectively) were recorded at the end of the dynamics every 2 fs for 4 ps and averaged over the simulation time t to calculate the corresponding velocity correlation function $g(t') = \frac{1}{N}\sum_t \sum_{i,a} m_a v_{i,a}(t)_{i,a}(t + t')$ as a function of the time-delay t'. The correlation function $g(t')$ was then Fourier-transformed $\tilde{g}(\omega) = \sum g(t')e^{-i\omega t'}$ and normalized, so providing the vibrational density of states $\rho(\omega) \propto \tilde{g}(\omega)$.

Raman spectroscopy

Raman spectra were recorded in the backscattering configuration using a Renishaw micro-Raman system with 20× objective and a 532 nm laser. The excitation powers were calculated according to the manufacturer's data. All measurements were performed in a Linkam Stage LTS 420, under constant N_2 flow and temperature control. The laser power was 30 mW focusing on a spot with a diameter of 1.6 μm yielding ca. 1.5e6 W/cm^2 in a full power mode. We used 10% of the full power to collect spectra without perturbing the material whereas 50% of the power was used to degrade the sample.

Raman spectra were analyzed by first subtracting the signal at a frequency higher than the excitation source to account for read-out noise. Pre-processing of the data was done using a Savitzky-Golay filtering method to remove signal noise. Baseline was determined by including several points along the spectrum which was fitted with a higher order polynomial line shape. Two criteria were met: (1) the selected points for the baseline fit did not coincide with any known vibrational peak of $MAPbI_3$ thin films, and (2) the same points were used for all spectra measured from the same sample at different moments in time.

Maximum power point tracker

For day-night cycling and the concentrated light test on devices, a high throughput maximum power point tracker (MPPT) was used. The MPPT was equipped with a metal halide lamp and a filter to generate a spectrum similar to global AM1.5 with an intensity of 100 mW/cm^2. During the tracking, the active area of the device was in contact with a heat pad in order to ensure direct thermal coupling and Peltier-elements were used for cooling. This temperature control was to ensure the measurement was done at standard testing condition, i.e., the cells at 25°C at all time. MPP tracking of devices was performed without encapsulation and under a continuous flow of nitrogen in a closed box. To generate 5.5 suns in Figure 6 in the main text, a Frensel lens was used to focus the light into a spot of 1 cm in diameter (the lens was at 5.5 cm away from the glass side of the device).

SUPPLEMENTAL INFORMATION

Supplemental information can be found online at https://doi.org/10.1016/j.joule.2022.06.029.

ACKNOWLEDGMENTS

N.P. thanks HyperCells—a joint research school between H.Z.B. and University of Potsdam. N.P. and A. Merdasa would like to thank Amran Al-Ashouri for insightful discussions during the project. A. Merdasa is grateful to Donatas Zigmantas for

illuminating insight into photoprotection mechanism in plants. The authors would like to acknowledge Hampus Näsström for his support during the aging measurement. The authors thank Ece Aktas and Silver-Hamill Turren-Cruz for their kind assistance on device and film fabrication used in this study. The authors thank Carola Klimm for acquiring SEM and EDX images. The authors are grateful to Malin Malmsjö, Rafi Sheikh, and Edouard Berrocal for assisting in the thermal-imaging measurements. J.A.S. thanks EPSRC and Prof. David Lidzey for PhD studentship funding via CDT-PV (EP/L01551X/1) and Erasmus+ for funding. S.M. thanks University of Ferrara for financial support for the project "Optimization of perovskite films" to the FIR program and PRACE for awarding him access to Marconi KNL and Marconi 100 at CINECA, Italy, through projects PROVING-IL (2019204911). A. Mattoni acknowledges MIUR for funding the project (grant no. 607 PON04a2 00490), M2M Netergit, and CNR for 2020 STM project 1352. M.S. thanks the German Research Foundation (DFG) for funding (SPP2196 and 431314977/GRK 2642); ProperPhotoMile, which is supported under the umbrella of SOLAR-ERA.NET Cofund 2 by the Spanish Ministry of Science and Education; the AEI (PCI2020-112185); CDTI (IDI-20210171); the Federal Ministry for Economic Affairs and Energy on the basis of a decision by the German Bundestag (FKZ 03EE1070B & FKZ 03EE1070A); and the Israeli Ministry of Energy (220-11-031). SOLAR-ERA.NET is supported by the European Commission within the EU Framework Programme for Research and Innovation HORIZON 2020 (Cofund ERA-NET Action, no. 786483). A. Merdasa acknowledges Lund Laser Center. E.U. and A. Merdasa acknowledge BMBF HyPerFORME project funding (grant 03XP0091).

AUTHOR CONTRIBUTIONS

N.P., S.M., A.A., and A. Merdasa conceived the idea and formulated the project and experiments. N.P. fabricated films and devices. A. Merdasa and N.P. performed PL studies with help from E.L.U. and I.G.S. A. Merdasa analyzed the PL data. J.L. provided samples and assisted during thermal-imaging measurements. A. Mattoni and S.M. computed all theoretical calculations. J.A.S., D.S., and J.B. performed the structural analysis by X-ray under the supervision of S.S. and C.G. L.C. and N.P. performed Raman measurements under the supervision of T.U. A. Merdasa and L.C. analyzed Raman results. M.S. contributed to the concentration PV measurements, contributed to the conceptualization of the study and revised the entire manuscript. H.K. and N.P. performed stability testing and analyzed the data. N.P., J.A.S., S.M., A.A., and A. Merdasa interpreted the data and wrote the manuscript with input from all authors.

DECLARATION OF INTERESTS

The authors declare no competing interests.

Received: June 6, 2021
Revised: February 15, 2022
Accepted: June 24, 2022
Published: July 25, 2022

REFERENCES

1. National Renewable Energy Laboratory (2020). PV efficiency chart. https://www.nrel.gov/pv/cell-efficiency.html.

2. Motti, S.G., Meggiolaro, D., Barker, A.J., Mosconi, E., Perini, C.A.R., Ball, J.M., Gandini, M., Kim, M., De Angelis, F., and Petrozza, A. (2019). Controlling competing photochemical reactions stabilizes perovskite solar cells. Nat. Photonics *13*, 532–539.

3. Domanski, K., Roose, B., Matsui, T., Saliba, M., Turren-Cruz, S.-H., Correa-Baena, J.-P., Carmona, C.R., Richardson, G., Foster, J.M., De Angelis, F., et al. (2017). Migration of cations induces reversible performance losses over day/night cycling in perovskite solar cells. Energy Environ. Sci. *10*, 604–613.

4. Khenkin, M.V., Anoop, K.M., Visoly-Fisher, I., Kolusheva, S., Galagan, Y., Di Giacomo, F.,

Vukovic, O., Patil, B.R., Sherafatipour, G., Turkovic, V., et al. (2018). Dynamics of photoinduced degradation of perovskite photovoltaics: From reversible to irreversible processes. ACS Appl. Energy Mater. *1*, 799–806.

5. Huang, F., Jiang, L., Pascoe, A.R., Yan, Y., Bach, U., Spiccia, L., and Cheng, Y.-B. (2016). Fatigue behavior of planar $CH_3NH_3PbI_3$ perovskite solar cells revealed by light on/off diurnal cycling. Nano Energy *27*, 509–514.

6. Rothmann, M.U., Kim, J.S., Borchert, J., Lohmann, K.B., O'Leary, C.M., Sheader, A.A., Clark, L., Snaith, H.J., Johnston, M.B., Nellist, P.D., and Herz, L.M. (2020). Atomic-scale microstructure of metal halide perovskite. Science *370*, eabb5940.

7. Akbulatov, A.F., Frolova, L.A., Tsarev, S.A., Zhidkov, I., Luchkin, S.Y., Kurmaev, E.Z., Stevenson, K.J., Aldoshin, S.M., and Troshin, P.A. (2020). Film deposition techniques impact the defect density and photostability of MAPbI 3 perovskite films. J. Phys. Chem. C *124*, 21378–21385.

8. Dall'Osto, L., Cazzaniga, S., Bressan, M., Paleček, D., Žídek, K., Niyogi, K.K., Fleming, G.R., Zigmantas, D., and Bassi, R. (2017). Two mechanisms for dissipation of excess light in monomeric and trimeric light-harvesting complexes. Nat. Plants *3*, 17033.

9. Takahashi, S., and Badger, M.R. (2011). Photoprotection in plants: a new light on photosystem II damage. Trends Plant Sci. *16*, 53–60.

10. Gollan, P.J., and Aro, E.-M. (2020). Photosynthetic signalling during high light stress and recovery: targets and dynamics. Philos. Trans. R. Soc. Lond. B Biol. Sci. *375*, 20190406.

11. Dar, M.I., Jacopin, G., Meloni, S., Mattoni, A., Arora, N., Boziki, A., Zakeeruddin, S.M., Rothlisberger, U., and Grätzel, M. (2016). Origin of unusual bandgap shift and dual emission in organic-inorganic lead halide perovskites. Sci. Adv. *2*, e1601156.

12. Selig, O., Sadhanala, A., Müller, C., Lovrincic, R., Chen, Z., Rezus, Y.L.A., Frost, J.M., Jansen, T.L.C., and Bakulin, A.A. (2017). Organic cation rotation and immobilization in pure and mixed methylammonium lead-halide perovskites. J. Am. Chem. Soc. *139*, 4068–4074.

13. Guo, R., Khenkin, M.V., Arnaoutakis, G.E., Samoylova, N.A., Barbé, J., Lee, H.K.H., Tsoi, W.C., and Katz, E.A. (2020). Initial stages of photodegradation of MAPbI3 perovskite: accelerated aging with concentrated sunlight. Sol. RRL *4*, 1–5.

14. Pisoni, A., Jaćimović, J., Barišić, O.S., Spina, M., Gaál, R., Forró, L., and Horváth, E. (2014). Ultra-low thermal conductivity in organic–inorganic hybrid perovskite $CH_3NH_3PbI_3$. J. Phys. Chem. Lett. *5*, 2488–2492.

15. Kovalsky, A., Wang, L., Guo, X., Dyck, J.S., and Burda, C. (2018). Temperature-dependent thermal conductivity study of MAPbI 3: using mild aging to reach a thermal percolation threshold for greatly improved heat transport. J. Phys. Chem. C *122*, 13243–13249.

16. Dualeh, A., Gao, P., Seok, S.Il., Nazeeruddin, M.K., and Grätzel, M. (2014). Thermal behavior of methylammonium lead-trihalide perovskite photovoltaic light harvesters. Chem. Mater. *26*, 6160–6164.

17. Song, Z., Watthage, S.C., Phillips, A.B., Tompkins, B.L., Ellingson, R.J., and Heben, M.J. (2015). Impact of processing temperature and composition on the formation of methylammonium lead iodide perovskites. Chem. Mater. *27*, 4612–4619.

18. Juarez-Perez, E.J., Hawash, Z., Raga, S.R., Ono, L.K., and Qi, Y. (2016). Thermal degradation of $CH_3NH_3PbI_3$ perovskite into NH_3 and CH_3I gases observed by coupled thermogravimetry-mass spectrometry analysis. Energy Environ. Sci. *9*, 3406–3410.

19. Merdasa, A., Bag, M., Tian, Y., Källman, E., Dobrovolsky, A., and Scheblykin, I.G. (2016). Super-resolution luminescence microspectroscopy reveals the mechanism of photoinduced degradation in $CH_3NH_3PbI_3$ perovskite nanocrystals. J. Phys. Chem. C *120*, 10711–10719.

20. Manser, J.S., and Kamat, P.V. (2014). Band filling with free charge carriers in organometal halide perovskites. Nat. Photonics *8*, 737–743.

21. Foley, B.J., Marlowe, D.L., Sun, K., Saidi, W.A., Scudiero, L., Gupta, M.C., and Choi, J.J. (2015). Temperature dependent energy levels of methylammonium lead iodide perovskite. Appl. Phys. Lett. *106*, 243904.

22. Futscher, M.H., Lee, J.M., McGovern, L., Muscarella, L.A., Wang, T., Haider, M.I., Fakharuddin, A., Schmidt-Mende, L., and Ehrler, B. (2019). Quantification of ion migration in $CH_3NH_3PbI_3$ perovskite solar cells by transient capacitance measurements. Mater. Horiz. *6*, 1497–1503.

23. Phung, N., Al-Ashouri, A., Meloni, S., Mattoni, A., Albrecht, S., Unger, E.L., Merdasa, A., and Abate, A. (2020). The role of grain boundaries on ionic defect migration in metal halide perovskites. Adv. Energy Mater. *10*, 1903735.

24. Ceratti, D.R., Cohen, A.V., Tenne, R., Rakita, Y., Snarski, L., Jasti, N.P., Cremonesi, L., Cohen, R., Weitman, M., Rosenhek-Goldian, I., et al. (2021). The pursuit of stability in halide perovskites: the monovalent cation and the key for surface and bulk self-healing. Mater. Horiz. *8*, 1570–1586.

25. Ceratti, D.R., Rakita, Y., Cremonesi, L., Tenne, R., Kalchenko, V., Elbaum, M., Oron, D., Potenza, M.A.C., Hodes, G., and Cahen, D. (2018). Self-healing Inside APbBr3 halide perovskite crystals. Adv. Mater. *30*, 1–7.

26. Galisteo-López, J.F., Calvo, M.E., and Míguez, H. (2019). Spatially resolved analysis of defect annihilation and recovery dynamics in metal halide perovskite single crystals. ACS Appl. Energy Mater. *2*, 6967–6972.

27. Merdasa, A., Tsarev, S., Akbulatov, A.F., Troshin, P., and Unger, E.L. (2020). Microscopic insight into the reversibility of photodegradation in $MAPbI_3$ thin films. J. Lumin. *219*, 116916.

28. Brivio, F., Frost, J.M., Skelton, J.M., Jackson, A.J., Weber, O.J., Weller, M.T., Goñi, A.R., Leguy, A.M.A., Barnes, P.R.F., and Walsh, A. (2015). Lattice dynamics and vibrational spectra of the orthorhombic, tetragonal, and cubic phases of methylammonium lead iodide. Phys. Rev. B *92*, 144308.

29. Meloni, S., Palermo, G., Ashari-Astani, N., Grätzel, M., and Rothlisberger, U. (2016). Valence and conduction band tuning in halide perovskites for solar cell applications. J. Mater. Chem. A *4*, 15997–16002.

30. Filip, M.R., Eperon, G.E., Snaith, H.J., and Giustino, F. (2014). Steric engineering of metal-halide perovskites with tunable optical band gaps. Nat. Commun. *5*, 5757.

31. Zhang, L., Geng, W., Tong, C.J., Chen, X., Cao, T., and Chen, M. (2018). Strain induced electronic structure variation in methyl-ammonium lead iodide perovskite. Sci. Rep. *8*, 7760.

32. Corrales, M.E., González-Vázquez, J., Balerdi, G., Solá, I.R., de Nalda, R., and Bañares, L. (2014). Control of ultrafast molecular photodissociation by laser-field-induced potentials. Nat. Chem. *6*, 785–790.

33. Juarez-Perez, E.J., Ono, L.K., Maeda, M., Jiang, Y., Hawash, Z., and Qi, Y. (2018). Photodecomposition and thermal decomposition in methylammonium halide lead perovskites and inferred design principles to increase photovoltaic device stability. J. Mater. Chem. A *6*, 9604–9612.

34. Abdelmageed, G., Mackeen, C., Hellier, K., Jewell, L., Seymour, L., Tingwald, M., Bridges, F., Zhang, J.Z., and Carter, S. (2018). Effect of temperature on light induced degradation in methylammonium lead iodide perovskite thin films and solar cells. Sol. Energy Mater. Sol. Cells *174*, 566–571.

35. Nickel, N.H., Lang, F., Brus, V.V., Shargaieva, O., and Rappich, J. (2017). Unraveling the light-induced degradation mechanisms of $CH_3NH_3PbI_3$ perovskite films. Adv. Electron. Mater. *3*, 1–9.

36. Quitsch, W.A., Dequilettes, D.W., Pfingsten, O., Schmitz, A., Ognjanovic, S., Jariwala, S., Koch, S., Winterer, M., Ginger, D.S., and Bacher, G. (2018). The role of excitation energy in photobrightening and photodegradation of halide perovskite thin films. J. Phys. Chem. Lett. *9*, 2062–2069.

37. Merdasa, A., Kiligaridis, A., Rehermann, C., Abdi-Jalebi, M., Stöber, J., Louis, B., Gerhard, M., Stranks, S.D., Unger, E.L., and Scheblykin, I.G. (2019). Impact of excess lead iodide on the recombination kinetics in metal halide perovskites. ACS Energy Lett. *4*, 1370–1378.

38. Wilson, J.N., Frost, J.M., Wallace, S.K., and Walsh, A. (2019). Dielectric and ferroic properties of metal halide perovskites. APL Mater. *7*, 010901.

39. Mattoni, A., and Caddeo, C. (2020). Dielectric function of hybrid perovskites at finite temperature investigated by classical molecular dynamics. J. Chem. Phys. *152*, 104705.

40. Mattoni, A., and Meloni, S. (2020). Defect dynamics in $MAPbI_3$ polycrystalline films: the trapping effect of grain boundaries. Helv. Chim. Acta *103*, e2000110.

41. Mattoni, A., Filippetti, A., Saba, M.I., and Delugas, P. (2015). Methylammonium rotational dynamics in lead halide perovskite

by classical molecular dynamics: the role of temperature. J. Phys. Chem. C *119*, 17421–17428.

42. Fabini, D.H., Laurita, G., Bechtel, J.S., Stoumpos, C.C., Evans, H.A., Kontos, A.G., Raptis, Y.S., Falaras, P., Van der Ven, A., Kanatzidis, M.G., et al. (2016). Dynamic stereochemical activity of the Sn^{2+} lone pair in perovskite $CsSnBr_3$. J. Am. Chem. Soc. *138*, 11820–11832.

43. Krumrey, M., and Ulm, G. (2001). High-accuracy detector calibration at the PTB four-crystal monochromator beamline. Nucl. Instrum. Methods Phys. Res. A *467–468*, 1175–1178.

44. Skroblin, D., Schavkan, A., Pflüger, M., Pilet, N., Lüthi, B., and Krumrey, M. (2020). Vacuum-compatible photon-counting hybrid pixel detector for wide-angle x-ray scattering, x-ray diffraction, and x-ray reflectometry in the tender x-ray range. Rev. Sci. Instrum. *91*, 023102.

45. Gottesman, R., Gouda, L., Kalanoor, B.S., Haltzi, E., Tirosh, S., Rosh-Hodesh, E., Tischler, Y., Zaban, A., Quarti, C., Mosconi, E., and De Angelis, F. (2015). Photoinduced reversible structural transformations in free-standing $CH_3NH_3PbI_3$ perovskite films. J. Phys. Chem. Lett. *6*, 2332–2338.

46. Pistor, P., Ruiz, A., Cabot, A., and Izquierdo-Roca, V. (2016). Advanced Raman spectroscopy of methylammonium lead iodide: development of a non-destructive characterisation methodology. Sci. Rep. *6*, 35973.

47. Xie, L.Q., Zhang, T.Y., Chen, L., Guo, N., Wang, Y., Liu, G.K., Wang, J.R., Zhou, J.Z., Yan, J.W., Zhao, Y.X., et al. (2016). Organic-inorganic interactions of single crystalline organolead halide perovskites studied by Raman spectroscopy. Phys. Chem. Chem. Phys. *18*, 18112–18118.

48. Udalova, N.N., Tutantsev, A.S., Chen, Q., Kraskov, A., Goodilin, E.A., and Tarasov, A.B. (2020). New features of photochemical decomposition of hybrid lead halide perovskites by laser irradiation. ACS Appl. Mater. Interfaces *12*, 12755–12762.

49. Khenkin, M.V., Anoop, K.M., Visoly-Fisher, I., Galagan, Y., Di Giacomo, F., Patil, B.R., Sherafatipour, G., Turkovic, V., Rubahn, H.-G.G., Madsen, M., et al. (2018). Reconsidering figures of merit for performance and stability of perovskite photovoltaics. Energy Environ. Sci. *11*, 739–743.

50. Lin, Q., Wang, Z., Snaith, H.J., Johnston, M.B., and Herz, L.M. (2018). Hybrid perovskites: prospects for concentrator solar cells. Adv. Sci. (Weinh) *5*, 1700792.

51. Wang, Z., Lin, Q., Wenger, B., Christoforo, M.G., Lin, Y.H., Klug, M.T., Johnston, M.B., Herz, L.M., and Snaith, H.J. (2018). High irradiance performance of metal halide perovskites for concentrator photovoltaics. Nat. Energy *3*, 855–861.

52. Demmig-Adams, B., and Adams, W.W. (1992). Photoprotection and other responses of plants to high light stress. Annu. Rev. Plant Physiol. Plant Mol. Biol. *43*, 599–626.

53. Powles, S.B. (1984). Photoinhibition of photosynthesis induced by visible light. Annu. Rev. Plant Physiol. *35*, 15–44.

54. Saliba, M., Correa-Baena, J.-P., Wolff, C.M., Stolterfoht, M., Phung, N., Albrecht, S., Neher, D., and Abate, A. (2018). How to make over 20% efficient perovskite solar cells in regular (n–i–p) and inverted (p–i–n) architectures. Chem. Mater. *30*, 4193–4201.

55. Al-Ashouri, A., Magomedov, A., Roß, M., Jošt, M., Talaikis, M., Chistiakova, G., Bertram, T., Márquez, J.A., Köhnen, E., Kasparavičius, E., et al. (2019). Conformal monolayer contacts with lossless interfaces for perovskite single junction and monolithic tandem solar cells. Energy Environ. Sci. *12*, 3356–3369.

56. Li, J., Dagar, J., Shargaieva, O., Flatken, M.A., Köbler, H., Fenske, M., Schultz, C., Stegemann, B., Just, J., Többens, D.M., et al. (2021). 20.8% Slot-die coated MAPbI 3 perovskite solar cells by optimal DMSO-content and age of 2-ME based precursor inks. Adv. Energy Mater. *11*, 2003460.

57. Ashiotis, G., Deschildre, A., Nawaz, Z., Wright, J.P., Karkoulis, D., Picca, F.E., and Kieffer, J. (2015). The fast azimuthal integration Python library: pyFAI. J. Appl. Crystallogr. *48*, 510–519.

58. Yavari, M., Ebadi, F., Meloni, S., Wang, Z.S., Yang, T.C.J., Sun, S., Schwartz, H., Wang, Z., Niesen, B., Durantini, J., et al. (2019). How far does the defect tolerance of lead-halide perovskites range? The example of Bi impurities introducing efficient recombination centers. J. Mater. Chem. A *7*, 23838–23853.

59. Perdew, J.P., Burke, K., and Ernzerhof, M. (1996). Generalized gradient approximation made simple. Phys. Rev. Lett. *77*, 3865–3868.

60. Umari, P., Mosconi, E., and De Angelis, F. (2014). Relativistic GW calculations on $CH_3NH_3PbI_3$ and $CH_3NH_3SnI_3$ perovskites for solar cell applications. Sci. Rep. *4*, 4467.

61. Ashari-Astani, N., Meloni, S., Salavati, A.H., Palermo, G., Grätzel, M., and Rothlisberger, U. (2017). Computational characterization of the dependence of halide perovskite effective masses on chemical composition and structure. J. Phys. Chem. C *121*, 23886–23895.

62. Lee, K., Murray, É.D., Kong, L., Lundqvist, B.I., and Langreth, D.C. (2010). Higher-accuracy van der Waals density functional. Phys. Rev. B *82*, 081101.

63. Shi, T., Yin, W.-J., and Yan, Y. (2014). Predictions for p-type $CH_3NH_3PbI_3$ perovskites. J. Phys. Chem. C *118*, 25350–25354.

64. Rappe, A.M., Rabe, K.M., Kaxiras, E., and Joannopoulos, J.D. (1990). Optimized pseudopotentials. Phys. Rev. B Condens. Matter *41*, 1227–1230.

65. Monkhorst, H.J., and Pack, J.D. (1976). Special points for Brillouin-zone integrations. Phys. Rev. B *13*, 5188–5192.

66. Cohen, A.V., Egger, D.A., Rappe, A.M., and Kronik, L. (2019). Breakdown of the static picture of defect energetics in halide perovskites: the case of the Br vacancy in $CsPbBr_3$. J. Phys. Chem. Lett. *10*, 4490–4498.

67. Freysoldt, C., Neugebauer, J., and Van de Walle, C.G. (2009). Fully ab initio finite-size corrections for charged-defect supercell calculations. Phys. Rev. Lett. *102*, 016402.

68. Giannozzi, P., Baroni, S., Bonini, N., Calandra, M., Car, R., Cavazzoni, C., Ceresoli, D., Chiarotti, G.L., Cococcioni, M., Dabo, I., et al. (2009). QUANTUM ESPRESSO: a modular and open-source software project for quantum simulations of materials. J. Phys. Condens. Matter *21*, 395502.

69. Wang, J., Wolf, R.M., Caldwell, J.W., Kollman, P.A., and Case, D.A. (2004). Development and testing of a general amber force field. J. Comput. Chem. *25*, 1157–1174.

70. Caddeo, C., Melis, C., Saba, M.I., Filippetti, A., Colombo, L., and Mattoni, A. (2016). Tuning the thermal conductivity of methylammonium lead halide by the molecular substructure. Phys. Chem. Chem. Phys. *18*, 24318–24324.

71. Mattoni, A., Filippetti, A., Saba, M.I., Caddeo, C., and Delugas, P. (2016). Temperature evolution of methylammonium trihalide vibrations at the atomic scale. J. Phys. Chem. Lett. *7*, 529–535.

72. Plimpton, S. (1995). Fast parallel algorithms for short-range molecular dynamics. J. Comput. Phys. *117*, 1–19.